Navier-Stokes Computations of Projectile Base Flow with and without Mass Injection

Jubaraj Sahu* and Charles J. Nietubicz*
U.S. Army Ballistic Research Laboratory, Aberdeen Proving Ground, Maryland
and
Joseph L. Steger†
Stanford University, Palo Alto, California

A computational capability has been developed for predicting the flowfield about projectiles, including the recirculatory base flow at transonic speeds. In addition, the developed code allows mass injection at the projectile base and hence is used to show the effects of base bleed on base drag. Computations have been made for a secant-ogive-cylinder projectile for a series of Mach numbers in the transonic flow regime. Computed results show the qualitative and quantitative nature of base flow with and without base bleed. Base drag is computed and compared with the experimental data and semiempirical predictions. The reduction in base drag with base bleed is clearly predicted for various mass injection rates. Results are also presented that show the variation of total aerodynamic drag both with and without mass injection for Mach numbers of $0.9 < M < 1.2$. The results obtained indicate that, with further development, this computational technique may provide useful design guidance for projectiles.

I. Introduction

A MAJOR area of concern in shell design is the accurate prediction of the total aerodynamic drag. Both the range and terminal velocity of a projectile (two critical factors in shell design) are directly related to the total aerodynamic drag. The total drag for projectiles can be divided into three components: 1) pressure drag (excluding the base region), 2) viscous (skin friction) drag, and 3) base drag. At transonic speeds, base drag constitutes a major portion of the total drag. For a typical shell at $M = 0.90$, the relative magnitudes of the aerodynamic drag components are: 20% pressure drag, 30% viscous drag, and 50% base drag.

The critical aerodynamic behavior of projectiles, indicated by rapid changes in the aerodynamic coefficients, occurs in the transonic speed regime and can be attributed in part to the complex shock structure existing on projectiles at transonic speeds. Therefore, in order to predict the total drag for projectiles, computation of the full flowfield (including the base flow) must be made. There are few reliable semiempirical procedures that can be used to predict shell drag; however, these procedures cannot predict the effects of mass injection. The objective of this research effort was to develop a numerical capability, using the Navier-Stokes computational technique, to compute the flowfield in the base region of projectiles at transonic speeds and thus to be able to compute the total aerodynamic drag with and without mass injection.

The pressure and viscous components of drag generally cannot be reduced significantly without adversely affecting the stability of the shell. Therefore, recent attempts to reduce the total drag have been directed toward reducing the base drag. A number of studies have been made to examine the total drag reduction due to the addition of a boattail.[1] Although this is very effective in reducing the total drag, it has a negative impact on the aerodynamic stability, especially at transonic velocities. An excellent review of the effect of boattailing on total drag and base pressure is presented in Ref. 1.

Another effective means of reducing the base drag is that of "base bleed" or "mass injection." In this method, a small amount of mass is injected into the base region to increase the base pressure and thus reduce the base drag. Recent range and precision tests[2] of a 155 mm projectile with and without base bleed have been conducted and an 85% reduction in base drag was obtained. Presently, the XM864 is an active projectile design that uses the base bleed concept for increased range. This concept of mass injection at the projectile base has been widely studied for supersonic flows,[3,4] while fewer data are available in the transonic flow regime.[5] Only very recently, with the advent of laser Doppler velocimeter (LDV) instrumentation, are extensive base flow data becoming available.

Recently, Navier-Stokes solvers[6,7] have been used to compute the aft end flowfield of axisymmetric bodies at supersonic velocities. Limited computational work has also been reported recently by Sullins et al.[8] on the numerical computations of the base region flow of a supersonic combustion ramjet engine using two-dimensional Navier-Stokes equations. At transonic speeds, a limited study of the flow past a boattailed afterbody has been performed by Chow et al.[9] using the coupled inviscid and boundary-layer formulations. Recent papers[10,11] have described the development and application of a thin-layer Navier-Stokes computational code to predict the transonic flow about slender bodies of revolution. In Refs. 10 and 11, the technique was shown to be a viable computational tool for predicting both external and internal flows for spinning and nonspinning projectiles of various geometric shapes. However, these calculations modeled the base flow as an extended sting and thus the base pressure and recirculatory base flow were not computed.

This paper describes a unique flowfield segmentation procedure[12,13] that has greatly simplified the development of the computer code for the simulation of the complete projectile with base. The code is used here to predict the base pressure of the shell at transonic speeds, including the effect of base bleed. Computed results show the quantitative and qualitative details of the base flow structure. The technique used computes the full flowfield over the projectile at transonic speeds; therefore, all three components of the total drag (pressure,

---

Received April 24, 1984; revision received Oct. 30, 1984. This paper is declared a work of the U.S. Government and therefore is in the public domain.

*Aerospace Engineer. Member AIAA.

†Associate Professor, Department of Aeronautics and Astronautics; presently, Senior Staff Scientist, NASA Ames Research Center, Moffett Field, Calif. Member AIAA.

viscous, and base drag) are computed. This computational technique is then applied to predict the effects of base bleed on the base drag reduction at transonic speeds. However, the combined effect of boattailing and base bleed is not considered here.

A brief description of the governing equations is given in Sec. II. A novel flowfield segmentation procedure, equivalent to using multiple adjoining grids, is used and described along with the computational technique in Sec. III. In Sec. IV, results are shown for transonic base pressure computations for a 6-caliber secant-ogive-cylinder shape for $0.9 < M < 1.2$ and $\alpha = 0$, with and without base bleed. The results show that the computational technique can be used to predict the base flow of projectiles with and without base bleed.

II. Formulation and Governing Equations

The objective is to compute the transonic flow over a projectile shape with a blunt base. Although the entire projectile flow is computed, the emphasis here is on the flowfield in the base region of the projectile. The present work deals with the numerical computation of the base flow, both with and without base bleed. Figure 1 shows a schematic illustration of the base region flowfield. The dividing streamline separates the recirculary base flow from the primary external flow. The flowfield is dominated by separation and mixed regions of locally supersonic and subsonic flows. In the base bleed case, a small amount of air is injected at the projectile base in a direction parallel to the primary flow. The injection at the base can be concentrated at the center of the base or spread throughout the entire base. In the present work, the injection takes place over 90% of the base.

The complete set of time-dependent generalized axisymmetric thin-layer Navier-Stokes equations is solved numerically to obtain a solution to this problem. The numerical technique used is an implicit finite difference scheme. Although time-dependent calculations are made, the transient flow is not of primary interest at the present time. The steady flow is the desired result, which is obtained in a time asymptotic fashion.

The azimuthal invariant (or generalized axisymmetric) thin-layer Navier-Stokes equations for curvilinear coordinates ξ, η, and ζ can be written as[6]

$$\frac{\partial \hat{q}}{\partial \tau} + \frac{\partial \hat{E}}{\partial \xi} + \frac{\partial \hat{G}}{\partial \zeta} + \hat{H} = Re^{-1}\frac{\partial \hat{S}}{\partial \zeta} \tag{1}$$

In Eq. (1), the thin-layer approximation is used and restrictions for axisymmetric flow (with or without spin) are imposed. The vector $\hat{q}$ contains all of the dependent variables, i.e., $\hat{q} = (\rho, \rho u, \rho v, \rho w, e)^T$. The transformed flux vectors $\hat{E}$ and $\hat{G}$ are linear combinations of the Cartesian flux vectors, e.g., $E = (\xi_x E + \xi_z G)/J$, where J is the Jacobian of transformation. The source term $\hat{H}$ results from assuming invariance in the azimuthal direction, while the viscous terms are contained in the vector $\hat{S}$.

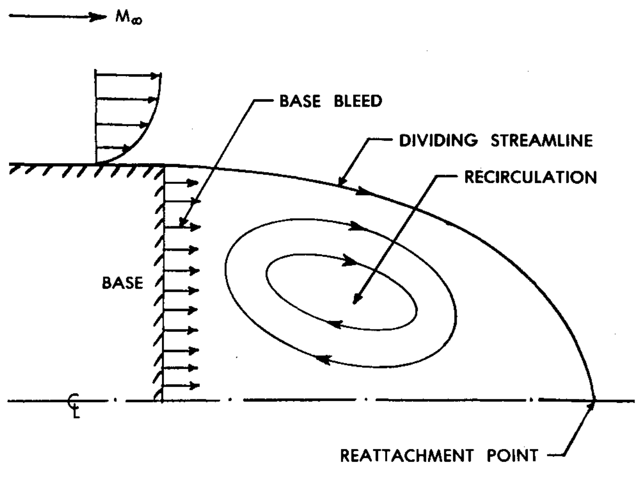

Fig. 1 Schematic of base region flowfield.

While Eq. (1) contains only two spatial derivatives, it retains all three momentum equations, thus allowing a degree of generality over the standard axisymmetric equations. In particular, the circumferential velocity is not assumed to be zero, thus allowing computations for spinning projectiles or swirl flow to be accomplished.

III. Numerical Method

Computational Algorithm

The azimuthal thin-layer Navier-Stokes equations are solved using an implicit approximate factorization finite difference scheme in delta form.[14] An implicit method was chosen because, for viscous flow problems, it permits a time step much greater than that allowed by explicit schemes. The Beam-Warming implicit algorithm has been used in various applications[6,10-17] for the equations in general curvilinear coordinates. The algorithm can be first- or second-order accurate in time and second- or fourth-order accurate in space. The equations are factored (spatially split), which reduces the solution process to one-dimensional problems at a given time level. Central difference operators are employed and the algorithm produces block tridiagonal systems for each space coordinate. The main computational work is contained in the solution of these block tridiagonal systems of equations.

Finite Difference Equations

The resulting finite difference equations, written in delta form, are

$$\begin{aligned}&\left(I + h\delta_\xi \hat{A}^n - \epsilon_I J^{-1}\nabla_\xi \Delta_\xi J\right)\left(I + h\delta_\zeta \hat{C}^n - \epsilon_I J^{-1}\nabla_\zeta \Delta_\zeta J\right.\\&\quad \left.- hRe^{-1}\delta_\zeta J^{-1}\hat{M}^n J\right) \times \left(\hat{q}^{n+1} - \hat{q}^n\right) = -\Delta t\left(\delta_\xi \hat{E}^n + \delta_\zeta \hat{G}^n\right.\\&\quad \left.- Re^{-1}\delta_\zeta \hat{S}^n\right) - \Delta t\hat{H}^n - \epsilon_E J^{-1}\\&\quad \times \left[\left(\nabla_\xi \Delta_\xi\right)^2 + \left(\nabla_\zeta \Delta_\zeta\right)^2\right] J\hat{q}^n\end{aligned} \tag{2}$$

Here $h = \Delta t$, since only first-order accuracy in the time differencing is needed for the steady-state flows considered here. This choice corresponds to the Euler implicit time differencing. The δ represent the central difference operators and Δ and ∇ the forward and backward difference operators, respectively. The Jacobian matrices $\hat{A} = \partial \hat{E}/\partial \hat{q}$ and $C = \partial \hat{G}/\partial \hat{q}$, along with the coefficient matrix $\hat{M}$ obtained from the local time linearization of $\hat{S}$, are described in detail in Ref. 15. Fourth-order explicit ϵ_E and implicit ϵ_I numerical dissipation terms are incorporated into the differencing scheme to damp high-frequency growth and thus to control the nonlinear instabilities.

Flowfield Segmentation

In order to simulate a projectile including the base, we have used two adjoining grids. However, this has been accomplished by a unique flowfield segmentation procedure that has greatly simplified the development of the computer code for the simulation of a complete projectile with a base. As described below, our segmentation process allows the existing implicit finite difference algorithm to be applied to two grids by making modifications only in the treatment of the boundary conditions and the internal structure of the block tridiagonal matrix.

Figure 2 is a schematic illustration of the flowfield segmentation used to compute the entire projectile flowfield that includes the base flow. It shows how the two grids ABCD and AEFG in the physical plane are transformed into a single segmented grid in the computational domain. An important advantage of this segmentation procedure lies in the preservation of the sharp corner at the base, which allows easy blending of the computational meshes between the regions ABCD and AEFG. No approximation of the actual sharp corner at the base is made. Thus, realistic representation of the base is inherent in the current procedure. The cross-hatched region represents the projectile. The line BC is the projectile base and the region ABCD is the base or wake region. The line AB is a computational cut through the physical base region that acts as a repetitive boundary in the computational domain.

With the computational domain so segmented, implicit integration of Eq. (2) is carried out in both the ξ and ζ directions (see Fig. 2) by solving the block tridiagonal matrices first in ξ and then in ζ. Note the presence of the lines BC (the base) and EF (nose axis) in the computational domain. Both lines act as boundaries in the computational domain and thus must be imposed upon the block tridiagonal matrix in the ξ direction. This is readily accomplished by initially ignoring these boundaries and then overwriting the tridiagonal elements. If these boundaries are ignored, the block tridiagonal matrix in the ξ direction (after setting $\epsilon_I = 0$ to simplify the illustration) is as follows:

$$\begin{bmatrix}
 & I & A_3 & & & & & \\
-A_2 & I & A_4 & & & & & \\
\ddots & \ddots & \ddots & & & & & \\
 & -A_{JB-2} & I & A_{JB} & & & & \\
 & \ddots & \ddots & \ddots & & & & \\
 & & -A_{JB-1} & I & A_{JB+1} & & & \\
 & & \ddots & \ddots & \ddots & & & \\
 & & & -A_{JB} & I & A_{JB+2} & & \\
 & & & \ddots & \ddots & \ddots & & \\
 & & & & -A_{JB+1} & I & A_{JB+3} & \\
 & & & & \ddots & \ddots & \ddots & \\
 & & & & & -A_{J\mathrm{MAX}-2} & I &
\end{bmatrix}
\begin{bmatrix}
\Delta q_2 \\ \Delta q_3 \\ \vdots \\ \vdots \\ \vdots \\ \Delta q_{JB} \\ \vdots \\ \Delta q_{JB+1} \\ \vdots \\ \vdots \\ \vdots \\ \Delta q_{J\mathrm{MAX}-1}
\end{bmatrix}^n
=
\begin{bmatrix}
RHS_2 \\ RHS_3 \\ \vdots \\ \vdots \\ \vdots \\ RHS_{JB} \\ \vdots \\ RHS_{JB+1} \\ \vdots \\ \vdots \\ \vdots \\ RHS_{J\mathrm{MAX}-1}
\end{bmatrix} \tag{3}$$

where A denotes the quantity $(\Delta t/2\Delta\xi)\hat{A}$ and I a 5×5 identity matrix. As a result of the flowfield segmentation procedure, the block tridiagonal matrix in the ξ direction has elements at $J = JB, JB+1$ that are treated as internal boundaries in the computational domain ($J = JB$ represents the projectile base, line BC, and $J = JB+1$ is the nose axis, line EF). Thus, the block tridiagonal matrix in the ξ direction given by Eq. (3) must be changed to take the following form:

$$\begin{bmatrix}
 & I & A_3 & & & & \\
-A_2 & I & A_4 & & & & \\
\ddots & \ddots & \ddots & & & & \\
 & -A_{JB-2} & I & A_{JB} & & & \\
 & 0 & I & 0 & & & \\
 & & 0 & I & 0 & & \\
 & & & -A_{JB+1} & I & A_{JB+3} & \\
 & & & \ddots & \ddots & \ddots & \\
 & & & & -A_{J\mathrm{MAX}-2} & I &
\end{bmatrix}
\begin{bmatrix}
\Delta q_2 \\ \Delta q_3 \\ \vdots \\ \vdots \\ \Delta q_{JB} \\ \Delta q_{JB+1} \\ \vdots \\ \vdots \\ \Delta q_{J\mathrm{MAX}-1}
\end{bmatrix}^n
=
\begin{bmatrix}
RHS_2 \\ RHS_3 \\ \vdots \\ \vdots \\ 0 \\ 0 \\ \vdots \\ \vdots \\ RHS_{J\mathrm{MAX}-1}
\end{bmatrix} \tag{4}$$

Note the appearance of two uncoupled block tridiagonals. At rows JB and $JB+1$, the variables $\Delta q^n = q^{n+1} - q^n$ are left unaltered and are later updated explicitly at the end of the inversions. These changes were easily implemented into an existing code in a modular fashion. One simply fills the block tridiagonal matrix, ignoring the base JB and the nose axis $JB+1$. The elements in these rows are then overloaded as shown above. The flowfield segmentation does not affect the block tridiagonal matrix in the ζ direction.

Implementation of Boundary Conditions

The no slip boundary condition for viscous flow is enforced by setting the contravariant velocities to zero, i.e.,

$$U = V = W = 0 \tag{5}$$

on the projectile surface. The flowfield in the immediate near-wake region has been considered to be weakly viscous and inviscid boundary conditions are used at the base. The viscous terms near the projectile surface and across the shear layer are considered to be the most dominant and have been retained within the thin-layer approximation used here. This approximation neglects the viscous terms normal to the base that are believed to be less significant. The recirculation region, which has a predominant effect on the base pressure, is in part set up by the viscously dominated shear layer.

The number of points used for this calculation resulted in a rather coarse grid in the near-wake region. However, the no-slip boundary conditions were tried on the coarse grid and the resulting changes in the flowfield were insignificant. Imposing these

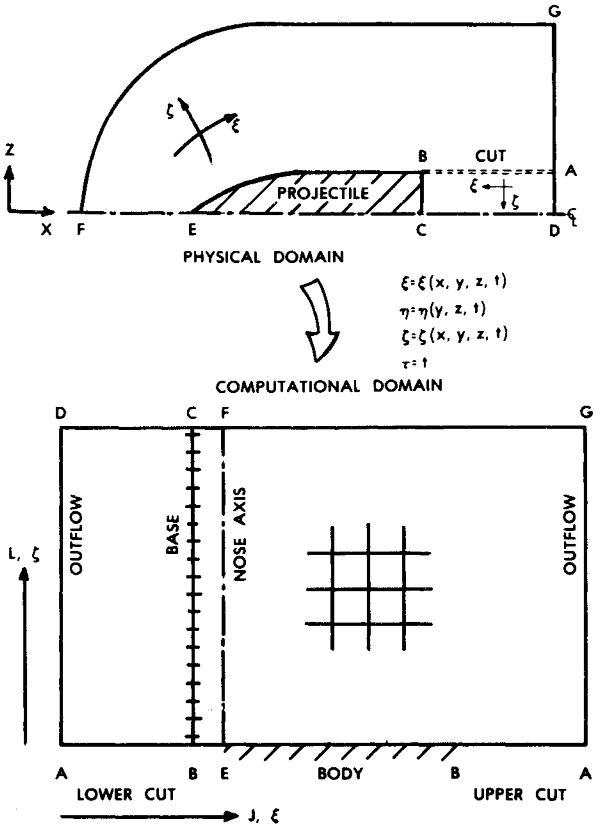

Fig. 2 Schematic of flowfield segmentation.

boundary conditions should have resulted in a large effect on the solution if the flowfield in the base region was viscously dominated. This lends support for the flowfield to be considered weakly viscous in the immediate near wake; thus, the inviscid boundary conditions at the base are justified. Additionally, at the corner of the base, the boundary conditions are double valued and depend on the direction from which the corner is approached. Approaching it in the streamwise direction (EB), the no-slip boundary condition is used; approaching it in the radial direction (along the base, CB), the inviscid boundary condition procedure is used.

Along the computational cut (line AB), the flow variables above and below the cut were simply averaged to determine the boundary conditions on the cut. On the centerline of the wake region (line CD), a symmetry condition is imposed. Freestream conditions are used at the outer boundary (FG of Fig. 2). Simple extrapolation for all of the flow variables is used at the downstream boundary (lines AD and AG) because, for transient calculations, use of a specified outflow pressure can give rise to numerical oscillations and even instability. A combination of extrapolation and symmetry is used on the nose axis (line EF).

Finally, to impose mass at the projectile base, u, v, and ρ are specified and $\partial w/\partial x$ is set to zero. The amount of air injected into the base region is specified by the mass flow rate $\dot{m}_j$. Since ρ_j and A_j are known, u_j can be calculated for any given mass flow rate. Rather than specifying $\dot{m}_j$, however, it is customary to specify a mass injection parameter I, where $I = \dot{m}_j/\rho_\infty u_\infty A$. In the next section, most of the results with base bleed are presented in terms of this parameter.

Turbulence Model

For the computation of turbulent flows, a turbulence model must be supplied. In the present calculations, a two-layer algebraic eddy viscosity model due to Baldwin and Lomax[17] is used. In their two-layer model, the inner region follows the Prandtl-Van Driest formulation. The outer formulation can be used in attached and separated boundary layers and with minor modifications in wakes as well. In both the inner and outer formulations, the distribution of vorticity is used to determine the length scales, thereby avoiding the necessity of finding the outer edge of the boundary layer (or wake). The magnitude of the local vorticity for the axisymmetric formulation is given by

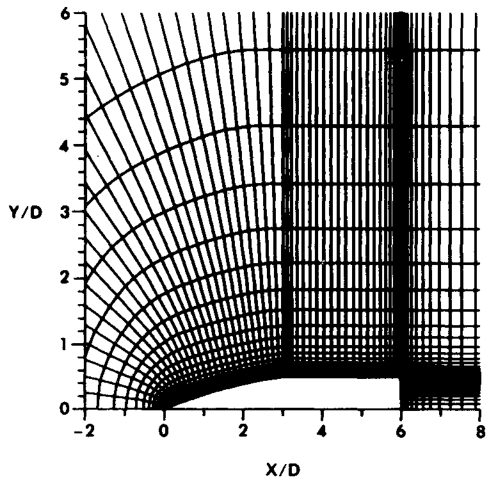

Fig. 3 Expanded grid in the vicinity of the projectile.

$$|\omega| = \sqrt{\left(\frac{\partial v}{\partial x}\right)^2 + \left(\frac{\partial v}{\partial z} - \frac{\partial w}{\partial y}\right)^2 + \left(\frac{\partial w}{\partial x} - \frac{\partial u}{\partial z}\right)^2} \tag{6}$$

In determining the outer length scale the function,[17]

$$F(y) = y|\omega|[1 - \exp(-y^+/A^+)] \tag{7}$$

is used where y^+ and A^+ are the conventional boundary-layer terms. For the base or wake flow, a few minor modifications are made in the model. The exponential term of Eq. (7) is set to zero. In other words, the Van Driest damping term is not applicable and is thus neglected. The outer formulation also requires the computation of the Klebanoff intermittency function and a velocity scale U_{dif} given by

$$U_{\mathrm{dif}} = (u^2 + v^2 + w^2)^{\frac{1}{2}}_{\max} - (u^2 + v^2 + w^2)^{\frac{1}{2}}_{\min} \tag{8}$$

Both of the terms on the right-hand side of Eq. (8) are evaluated via the velocity profiles. For wall-bounded flows, the minimum term in U_{dif} is usually set to zero. For wakes, the Klebanoff intermittency factor is determined by measuring the distance from the centerline of symmetry. The outer length scales were arbitrarily increased or decreased by a factor of two and the base flow results were found to be insensitive to these changes. However, the algebraic eddy viscosity model may not be strictly valid for all of the wake flow situations. More realistic or complex turbulence models must be considered a subject left for future study.

Computational Grid

The finite difference grid used for the numerical computations was obtained from a grid generator described in Ref. 18. This program allows arbitrary grid point clustering, thus enabling the grid points of the projectile shapes to be clustered in the vicinity of the body surface. The grid consists of 108 points in the longitudinal direction and 50 points in the radial direction. Figure 3 shows an expanded view of the grid in the vicinity of the projectile. The computational domain extended to four body lengths in front, four body lengths in the radial direction, and four body lengths behind the base of the projectile. The grid points in the normal direction were exponentially stretched away from the surface with the minimum spacing at the wall of 0.00002D. This spacing locates at least two points within the laminar sublayer.

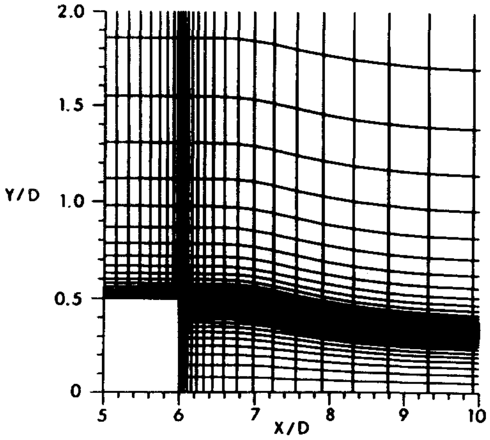

Fig. 4 Grid adapted to the shear layer.

The grid shown in Fig. 3 was generated in two segments. First, the grid in the outer region is obtained using an elliptic solver[18] for the ogive portion and straight-line rays for the remaining portion, which runs all the way to downstream boundary. Second, the grid in the base region is obtained simply by extending the straight lines perpendicular to line AB down to the centerline of symmetry (line CD). An exponential stretching with the minimum spacing of $0.00002D$ at line AB is used. It should be noted that the same minimum spacing $0.00002D$ is specified on both sides of the cut, thus maintaining a smooth variation of grid across the cut. This spacing could, of course, be increased downstream of the base. The number of grid points above and below line AB is the same (50 points), which ensures an adequate number of points in the base region. As can be seen in Fig. 3, the grid points are clustered near the nose-cylinder junction and at the projectile base where appreciable changes in flow variables are expected.

As indicated in Fig. 3, the fine viscous grid follows the cut labeled as AB in Fig. 2. Insofar as the viscous shear layer begins to neck-down shortly behind the base, much of this fine grid resolution is wasted. As a consequence, logic has been implemented to adjust the grid cut AB to the viscous shear layer. Such a grid is shown in Fig. 4 in which the height of the cut is weighted between a moment of shear and the standard nonadaptive grids. Specifically, the cut height $\bar{z}_j$ at each j location is determined by the relation

$$\bar{z}_j = \frac{\sum(\delta_z u_{Jl})^2 z_{Jl} + \epsilon D/2}{\sum(\delta_z u_{Jl})^2 + \epsilon} \tag{9}$$

where the l summation is carried out only for those points within an interval $0.2D \leq z_{Jl} \leq D/2$. Here D is the base diameter, δ_z a central difference operator, and ϵ a positive parameter that ensures a standard grid if all $\delta_z u_{JL}$ are zero or if ϵ is very large. Additional averaging is used in the x direction (longitudinal direction).

IV. Results

The model geometry used in the present study is shown in Fig. 5. The model consists of a 3-caliber secant-ogive nose and a 3-caliber cylinder.

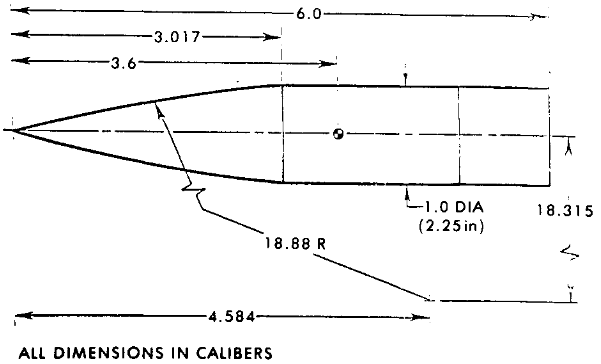

Fig. 5 Model geometry.

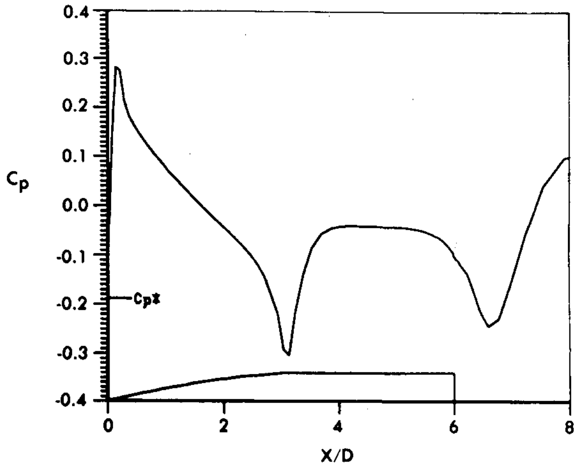

Fig. 6 Longitudinal surface pressure distribution, $M = 0.9$, $\alpha = 0$, $I = 0$ (without base bleed).

A series of computations have been made for this projectile at Mach numbers $0.9 < M < 1.2$ and $\alpha = 0$. Limited base pressure measurements were made by Kayser[19] for this projectile and are compared with the computed results. The projectile was supported by a base-mounted sting and measurements of base pressure were made at only one location along the base. These experiments were conducted at the Langley Research Center 8 ft Transonic Pressure Tunnel.[20] Computational base pressure results are also compared with available semiempirical data[21] and the results obtained from the data base on afterbody drag.[22] The results are presented in the form of surface pressure distributions, contour plots, and velocity vector plots.

The freestream Reynolds number for the series of computations was fixed at 4.5×10^6 based on the total model length. The computations were started from freestream conditions and marched in time to obtain the steady-state solution. The initial calculation was made for $M = 0.9$. Previous converged solutions were then used as starting conditions for additional Mach number runs to achieve faster convergence. The numerical solutions were converged when changes in the flowfield variables at all grid points were insignificant between prescribed time intervals. Additionally, the solution residuals were required to decrease by several orders of magnitude. After the solutions converged, the time step was reduced by an order of magnitude and additional runs were made. These runs showed no appreciable changes, which indicates that the flowfield in the base region was steady. The results are now presented for both cases: 1) base flow without injection and 2) base flow with injection.

Figures 6 and 7 show the distribution of the surface pressure coefficient C_p as a function of axial position without and with mass injection at the base, respectively. The value of C_p beyond $X/D = 6$ is the value of pressure coefficient along the line extending from the cylinder portion straight to the downstream boundary. In Fig. 6 there is no mass injection at the base. The pressure distribution reflects the shock pattern that typically occurs on shell at transonic velocities, the rapid expansion that occurs at the blunt base, and the recompression that occurs downstream of the base. The pressure coefficient distribution for a case with large mass addition is shown in Fig. 7. The previous rapid expansion at the base and recompression downstream of the base are seen to be virtually eliminated.

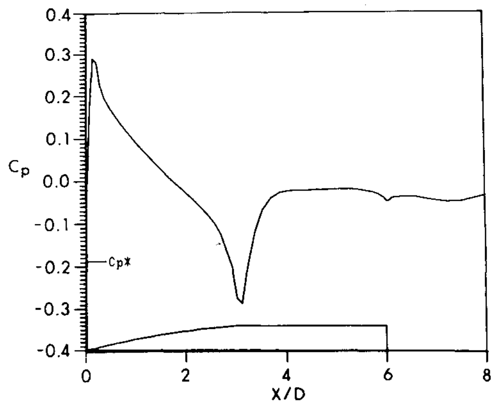

Fig. 7 Longitudinal surface pressure distribution, $M = 0.9$, $\alpha = 0$, $I = 0.13$ (with base bleed).

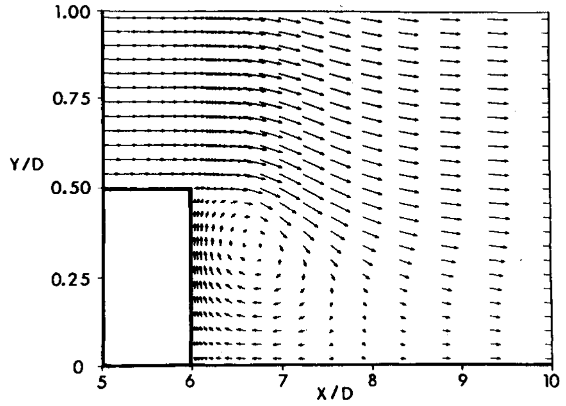

Fig. 8 Velocity vector field, $M = 0.9$, $\alpha = 0$, $I = 0$.

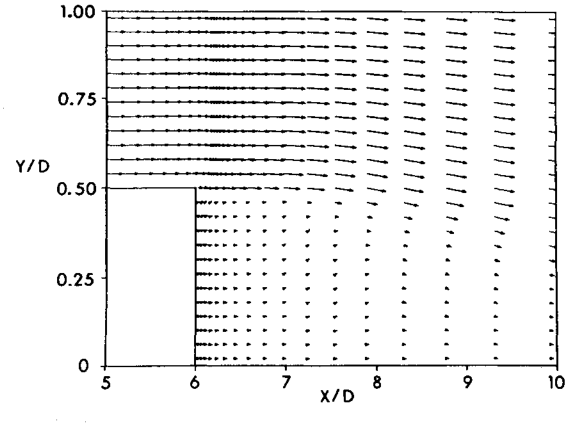

Fig. 9 Velocity vector field, $M = 0.9$, $\alpha = 0$, $I = 0.13$.

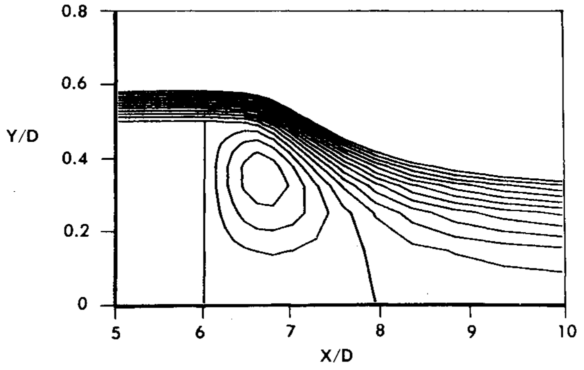

Fig. 10 Stream function contours, $M = 0.9$, $\alpha = 0$, $I = 0$.

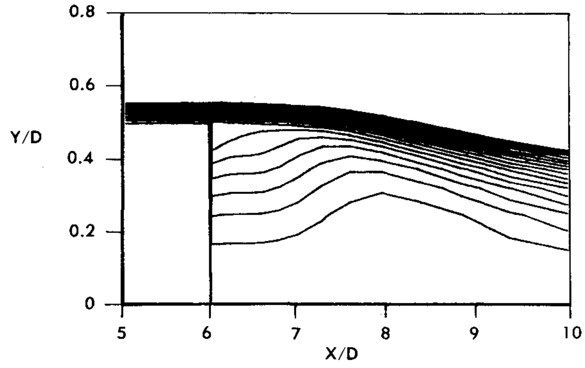

Fig. 11 Stream function contours, $M = 0.9$, $\alpha = 0$, $I = 0.13$.

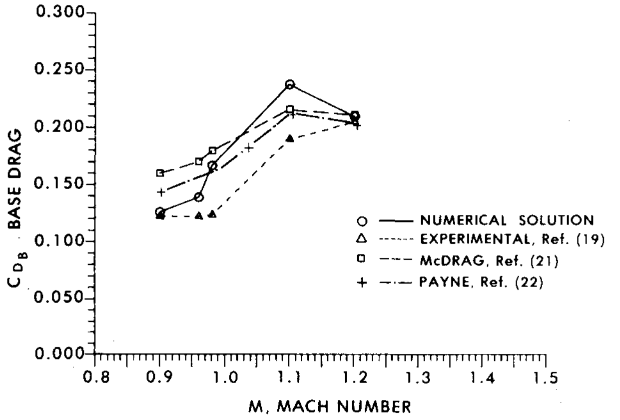

Fig. 12 Variation of base drag coefficient with Mach number, $\alpha = 0$.

Figure 8 shows the velocity vector field in the base region for $M = 0.9$, $\alpha = 0$, and $I = 0$. Each vector shows the magnitude and the direction of the velocity at that point. The figure shows the velocity field when there is no base bleed and the recirculatory flow in the base region is clearly evident. The velocity vector plot in Fig. 9 shows the effect of base bleed on the near-wake flowfield for a mass injection parameter, $I =$ 0.13. The flowfield in the base region has now been dramatically altered. The recirculation pattern has been totally swept downstream.

Figures 10 and 11 are stream function contour plots in the wake region, again for $M = 0.9$ and $\alpha = 0$. These figures are deliberately stretched in the y direction (not drawn to the same scale in x and y) to show the flow pattern in the base region as clearly as possible. Figure 10 is for the case of base flow with no mass injection at the base. It clearly shows the recirculation region and the position of the dividing streamline that separates the recirculatory base flow from the main flow. The reattachment point is about 2 calibers down from the base. Note the strong shear layer in the base region. Figure 11 shows the flow pattern in the base region with mass injection allowed at the base. For a mass injection parameter $I = 0.13$, its effect on the flowfield in the base region is apparent. The figure shows that dramatic change in the flowfield. The recirculation region has been eliminated and the shear layer has been displaced markedly.

A more critical check of the computational results is presented in Fig. 12 where the base drag is plotted as a function of Mach number. Computational results are indicated by circles, experimental results[19] by triangles, data base results[22] by diamonds, and the results obtained using a semiempirical technique developed by McCoy[21] by squares. The results from the data base are based on correlation of the base pressures obtained from a number of experiments and other analytical techniques. As expected, the base drag increases as the Mach number increases from 0.9 to 1.2. The semiempirical technique

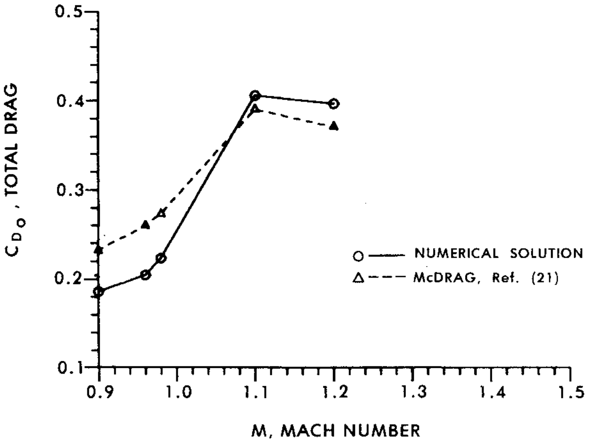

Fig. 13 Variation of total drag coefficient with Mach number, $\alpha = 0$.

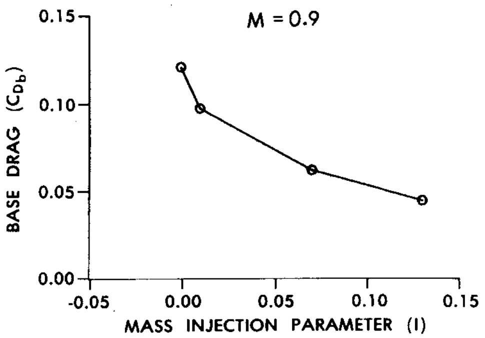

Fig. 14 Variation of base drag coefficient with base bleed, $M = 0.9$, $\alpha = 0$.

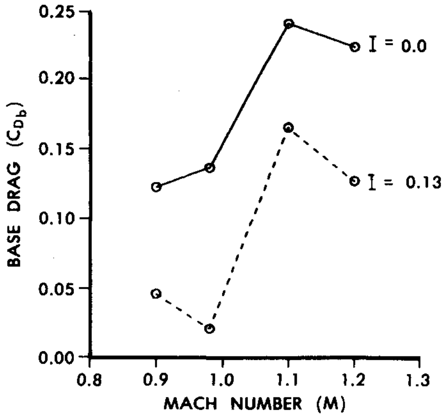

Fig. 15 Variation of base drag coefficient with Mach number, $\alpha = 0$ (with and without base bleed).

shows generally higher base drag when compared with computational and experimental results. The computational results predict the expected drag rise that occurs at $0.9 < M < 1.2$. The computational results, however, indicate a greater increase in drag than predicted by either the semiempirical code or the experimental measurements. The discrepancy between the numerical and the experimental results can partly be attributed to the fact that the experimental data was obtained with a sting attached to the base. The sting has an effect of weakening the recirculatory flow in the base region and leads to higher base pressure and hence lower base drag. The agreement between the computational and data base results is very satisfactory.

Since the entire projectile flowfield, including the base flow, has been computed, all three drag components have been computed and thus the total drag determined. Figure 13 shows the variation of the total aerodynamic drag with Mach number. As expected, the total drag increases as the Mach number increases from 0.9 to 1.2. The computational results are compared with the results obtained by semiempirical technique and are in satisfactory agreement.

Another critical look at the computational results is presented in Figs. 14 and 15. These figures show the quantitative details of projectile flowfield. Figure 14 shows the variation of base drag with mass injection rates for $M = 0.9$ and $\alpha = 0$. The reduction in base drag with base injection can be seen clearly. The percent reduction in base drag increases with the increase in the injection rate.

Figure 15 shows the variation of base drag with Mach number, with and without base injection. In this figure, the computational results without injection at the base are shown by the solid line, whereas the dotted line represents the computational results obtained with injection at the base. The reduction in base drag with base injection can be seen clearly. Figure 15 indicates that the percent reduction in base drag has increased with an increase in Mach number from 0.9 to 0.98. Additionally, the expected drag rise in the transonic speed regime is well predicted for $0.9 < M < 1.2$ and the reduction in base drag due to base bleed has been clearly demonstrated.

V. Summary

A promising computational capability has been developed that computes the full projectile flowfield, including the recirculatory base flow at transonic speeds both with and without mass injection.

Numerical computations have been made for Mach numbers $0.9 < M < 1.2$ to predict the base drag and the total drag with and without base bleed. Computed results show the qualitative features of the flowfield in the near wake for both cases. The calculations predict the expected drag rise that occurs from $0.9 < M < 1.2$. Quantitative comparisons of base drag and the total drag are in good agreement with experimental data and semiempirical predictions. For $M = 0.9$ and $\alpha = 0$, the percent reduction in base drag up to 60% was found with the increase in the injection rate. For a large mass injection rate, the reduction in base drag between 40-80% was observed for the entire range of transonic speeds, $0.9 < M < 1.2$.

References

[1] Sedney, R., "Review of Base Drag," U.S. Army Ballistic Research Laboratory, Aberdeen Proving Ground, Md., Rept. 1337, Oct. 1966 (AD 808767).

[2] "155mm ERFB Base Bleed Range and Precision Tests," Proof and Experimental Test Establishment, Nicolet, Quebec, for Space Research Corp., Jan. 11, 1978.

[3] Murthy, S.N.B. (ed.), *Progress in Astronautics and Aeronautics: Aerodynamics of Base Combustion*, Vol. 40, AIAA, New York, 1976.

[4] Dickinson, E.R., "The Effectiveness of Base-Bleed in Reducing Drag of Boattailed Bodies at Supersonic Velocities," U.S. Army Ballistic Research Laboratory, Aberdeen Proving Ground, Md., Memorandum Rept. 1244, 1960 (AD 234315).

[5] Sykes, D.M., "Cylindrical and Boattailed Afterbodies in Transonic Flow with Gas Ejection," *AIAA Journal*, Vol. 8, March 1970, pp. 588-589.

[6] Diewert, G.S., "A Computational Investigation of Supersonic Axisymmetric Flow over Boattails Containing a Centered Propulsive Jet," AIAA Paper 83-0462, Jan. 1983.

[7] Weinberg, B.C., McDonald, H., and Shamroth, S.J., "Navier-Stokes Computations of Aft End Flow Fields," Final Report, Army Research Office, Contract DAAG29-79-C-0003, May 1982.

[8] Sullins, G.A., Anderson, J.D., and Drummond, J.P., "Numerical Investigation of Supersonic Base Flow with Parallel Injection," AIAA Paper 82-1001, June 1982.

[9] Chow, W.L., Bober, L.J., and Angerson, B.H., "Strong Interaction Associated with Transonic Flow Past Boattails," *AIAA Journal*, Vol. 13, Jan. 1975, pp. 112-113.

[10] Nietubicz, C.J., Pulliam, T.H., and Steger, J.L., "Numerical Solution of the Azimuthal-Invariant Thin-Layer Navier-Stokes Equations," U.S. Army Ballistic Research Laboratory, Aberdeen Proving Ground,

Md., ARBRL-TR-02227, March 1980 (AD A085716). (See also AIAA Paper 79-0010, Jan. 1979.)

[11] Nietubicz, C.J., "Navier-Stokes Computations for Conventional and Hollow Projectile Shapes at Transonic Velocities," U.S. Army Ballistic Research Laboratory, Aberdeen Proving Ground, Md., ARBRL-MR-03184, July 1982 (AD A116866). (See also AIAA Paper 81-1262, June 1981.)

[12] Sahu, J., Nietubicz, C.J., and Steger, J.L., "Numerical Computation of Base Flow for a Projectile at Transonic Speeds," U.S. Army Ballistic Research Laboratory, Aberdeen Proving Ground, Md., ARBRL-TR-02495, June 1983 (AD A130293). (See also AIAA Paper 82-1358, Aug. 1982.)

[13] Sahu, J., Nietubicz, C.J., and Steger, J.L., "Navier-Stokes Computations of Projectile Base Flow with and without Base Injection," AIAA Paper 83-0224, Jan. 1983.

[14] Beam, R. and Warming, R.F., "An Implicit Factored Scheme for the Compressible Navier-Stokes Equations," *AIAA Journal*, Vol. 16, April 1978, pp. 393-402.

[15] Steger, J.L., "Implicit Finite Difference Simulation of Flow About Arbitrary Geometries with Application to Airfoils," *AIAA Journal*, Vol. 16, July 1978, pp. 679-686.

[16] Pulliam, T.H. and Steger, J.L., "On Implicit Finite-Difference Simulations of Three-Dimensional Flow," *AIAA Journal*, Vol. 18, Feb. 1980, pp. 159-167.

[17] Baldwin, B.S. and Lomax, H., "Thin-Layer Approximation and Algebraic Model for Separated Turbulent Flows," AIAA Paper 78-257, 1978.

[18] Steger, J.L., Nietubicz, C.J., and Heavey, K.R., "A General Curvilinear Grid Generation Program for Projectile Configurations," U.S. Army Ballistic Research Laboratory, Aberdeen Proving Ground, Md., ARBRL-MR-03142, Oct. 1981 (AD A107334).

[19] Kayser, L.D., Ballistic Research Laboratory, Aberdeen Proving Ground, Md., private communications.

[20] Kayser, L.D. and Whiton, F., "Surface Pressure Measurements on a Boattailed Projectile Shape at Transonic Speeds," U.S. Army Ballistic Research Laboratory, Aberdeen Proving Ground, Md., ARBRL-MR-03161, March 1982 (AD A113520).

[21] McCoy, R.L., "McDrag—A Computer Program for Estimating the Drag Coefficients of Projectiles," U.S. Army Ballistic Research Laboratory, Aberdeen Proving Ground, Md., ARBRL-TR-02293, Feb. 1981 (AD A098110).

[22] Payne, P.R. and Hartley, R.M., "Afterbody Drag, Volume 1—Drag of Conical and Circular Arc Afterbodies without Jet Flow," Final Rept. DTNSRDC/ASED-80/10, Bethesda, Md., May 1980.